Journal of Nuclear Materials 599 (2024) 155235

Contents lists available at ScienceDirect

Journal of Nuclear Materials

journal homepage: www.elsevier.com/locate/jnucmat

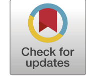

Damage microstructures in Ti_3SiC_2 under successive Xe-He-H ions irradiation and annealing process

Qing Chang [a,b], Qing Peng [c,d,e], Jiannan Hao [c], Pan Qi [f], Penghui Lei [g], Ni Jiang [a,b], Chao Ye [a,b,*]

[a] Institute of Clean Energy, Yangtze River Delta Research Institute, Northwestern Polytechnical University, Taicang 215400, China
[b] Science and Technology on Thermo structural Composite Materials Laboratory, Northwestern Polytechnical University, Xi'an, Shaanxi, 710072, China
[c] State Key Laboratory of Nonlinear Mechanics, Institute of Mechanics, Chinese Academy of Sciences, Beijing 100190, China
[d] Center of Materials Science and Optoelectronics Engineering, University of Chinese Academy of Sciences, Beijing, 100049, China
[e] Guangdong Aerospace Research Academy, Guangzhou, 511458, China
[f] China Nuclear Power Operation Technology Corporation (CNPO), LTD, Wuhan, 430223, China
[g] School of Nuclear Science and Technology, Xi'an Jiaotong University, Xi'an, China

HIGHLIGHTS

- Si-rich precipitates result in the differences of hardness in Ti_3SiC_2.
- Xe generates Si frenkel pairs while he enhances their recombination.
- Strip-like Si clusters are formed by emitting dislocation loops in TiC.

GRAPHICAL ABSTRACT

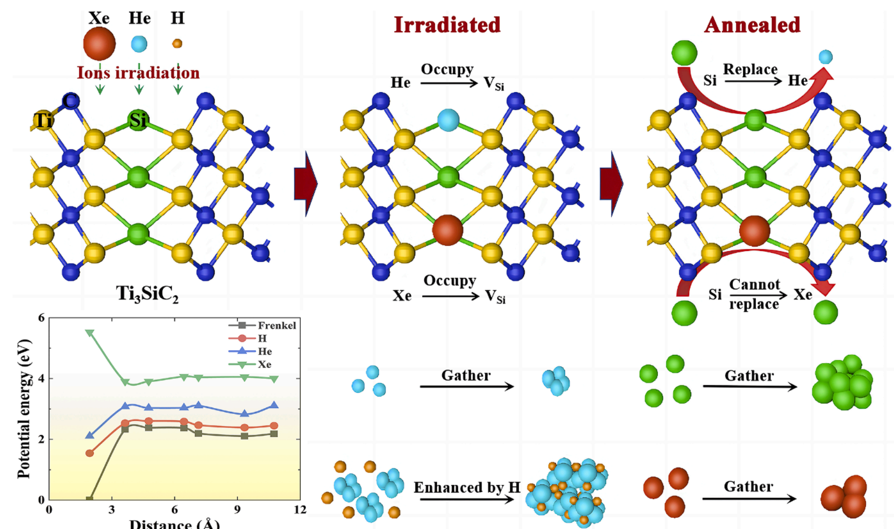

ARTICLE INFO

Keywords:
Ti_3SiC_2
Ion irradiation
Bubble
Si-rich precipitate
Nano-hardness

ABSTRACT

Ti_3SiC_2 is recognized as a promising candidate material for nuclear energy applications; however, the microstructural defects resulting from complex irradiation processes remain elusive. This study investigates the microstructural evolution of Ti_3SiC_2 under sequential Xe-He-H ions irradiation at room temperature, followed by annealing at 900 °C, employing both experimental and first-principles computational approaches. A reverse phase transformation occurred following He irradiation, indicating that He facilitates the remote migration and

* Corresponding author at: Institute of Clean Energy, Yangtze River Delta Research Institute, Northwestern Polytechnical University, Taicang 215400, China.
E-mail address: yechao@nwpu.edu.cn (C. Ye).

https://doi.org/10.1016/j.jnucmat.2024.155235
Received 28 February 2024; Received in revised form 8 June 2024; Accepted 13 June 2024
Available online 15 June 2024
0022-3115/© 2024 Elsevier B.V. All rights reserved, including those for text and data mining, AI training, and similar technologies.

recombination of Si vacancies through the formation of He-Si pairs during annealing. Post-annealing, the Xe-irradiated sample exhibited a widespread distribution of small Xe bubbles, whereas larger bubbles were prevalent at peak damage regions in the samples subjected to Xe+He and Xe+He+*H* irradiation. Concurrently, Si-rich precipitates with distinct distribution patterns were observed in samples irradiated with Xe, Xe+He, and Xe+He+*H* ions, significantly affecting the hardness. First-principles calculations reveal that the distinct damage profiles are primarily attributed to the dynamic behaviors of Si interstitials. The Ti-Si bonds are relatively weak and easily broken, leading to abundant Si interstitials in Xe ion irradiation, and He enhances Si diffusion. Conversely, H enhances Si segregation by preventing He from capturing Si interstitials. Within the TiC grains, He promotes Si migration, causing an approximately 700-fold increase in Si diffusivity at 900 °C. The Si segregation leads to the nucleation of ⟨110⟩ dislocation loops, culminating in the formation of distinctive strip-like Si clusters. This study elucidates the formation mechanism of Si segregation within Ti_3SiC_2, providing valuable insights for the design of irradiation-resistant materials.

1. Introduction

Generation IV innovative fission nuclear reactors, such as Gas Fast Reactor (GFR), are a hot research topic. Such reactors are designed to operate under high temperature (500–800 ℃ in normal conditions and up to 1600 ℃ in accidental scenarios), serious irradiation damage, aggressive corrosion, and high helium-pressure [1,2]. These extreme service environments pose significant challenges for materials used in reactors, which require them with outstanding irradiation resistance, excellent thermal conductivity, thermomechanical stability, and so on. In recent years, a new class of ternary layered carbides or nitrides named $M_{n+1}AX_n$ phase (commonly referred as MAX phase) have been widely investigated [3], where M refers to an early transition metal, such as Ti, Cr, V, etc.; A is an element from group A (mostly III A and IV A group); X is carbon and/or nitrogen; $n = 1$, 2 or 3, and the phases are named as 211, 312, 413 MAX phases, respectively. MAX phases show hexagonal crystal structure (P63/mmc), consisting of M_6X octahedra separated by A atomic layers [4]. Due to the unique ternary laminated structure, MAX phases exhibit the combination of typical properties from both ceramics and metals [5,6], including outstanding thermal properties, perfect corrosion resistance, and high temperature oxidation resistance [7,8]. For example, Ti_3SiC_2 is stable at temperatures as high as 1800 ℃ under an argon atmosphere [9], and most MAX phases have high thermal conductivity(for example, 40 W/m·K for Ti_3AlC_2 and 37 W/m·K for Ti_3SiC_2) [4], these excellent thermal properties make MAX phase have potential ability to be used in GFR applications.

MAX phases have outstanding irradiation resistance [10,11]. Ti_3SiC_2 remained crystalline structure after the 700 keV C^+ ions irradiation with a dose up to 60 dpa at 350 ℃ [12], and its structure has not been completely amorphized under 400 keV Xe ions irradiation with the dose up to 116.9 dpa at 500 ℃[13]. Moreover, plenty of interesting behaviors have been found in MAX phases under ion irradiation, such as phase transformation, anisotropic expansion, and microstructure change. For instance, 'black spots', antisite defect clusters, stacking faults, and nano-twin structures can be observed in Ti_3AlC_2 under heavy ions irradiation with high energy [14,15]. Wang [16-18] indicated that Ti_3AlC_2 irradiated with 3×10^{13} and 2×10^{16} Au ions/cm^2 at room temperature had a HCP-γ-FCC phase transformation, and the size of unique FCC-$(M_{n+1}A)X_n$ nanodomains increased when the dose was up to 300 dpa, which can be considered as another critical mode for MAX phases to facilitate irradiation tolerance. For volumetric swelling, although numerous works reveal that the anisotropic expansion of materials after irradiation is unavoidable, the expansion extent of MAX phases is much weaker than that of SiC. For example, the volume swelling of Ti_3SiC_2 is 2.2 ± 0.8 % while the α-SiC is 16.4 ± 1.3 % under the 4 MeV Au ions irradiation with a fluence of 10^{19} m^{-2} at room temperature [19]. Therefore, given the excellent mechanical stability in such extreme environment, MAX phases show great potential to be candidate materials in nuclear reactors.

For the practical applications of reactor cladding materials, it is necessary to consider the behaviors of helium and hydrogen atoms, which can be generated either by radiation or transmutation through (n, α) nuclear reaction. The accumulation of helium atoms would lead to the degradation of mechanical properties by means of void swelling, helium bubbles, and embrittlement. Some calculations [20,21] elucidate that Ti_3SiC_2 has better resistance to hydrogen embrittlement than metals, the unique Si layers in Ti_3SiC_2 has a self-healing ability in response to the radiation damage induced by helium atoms via acting as the channels for the accumulation, desorption, and transportation of helium atoms. At high temperature(>500 ℃), helium atoms can diffuse quickly into Si layer and the largest helium cluster formed in Si layer consists of no more than 7 helium atoms, only causing about 2 % volume swelling at most [22]. Zhang [23] demonstrated that the growth of helium bubbles was the main damage induced by He irradiation and the bubbles were mainly restricted in nano-laminate layers; when the annealing temperature increased from room temperature to 750 ℃, the size of helium bubbles grew from 1.4 nm to 10 nm; as the annealing temperature increased up to 1050 ℃, the helium bubbles transformed from spherical-like shape into platelet-like shape. In contrast, Su [24] proposed that small helium bubbles could grow into large bubbles without the help of capture assistance from nano-laminate layers in Ti_3SiC_2 after being annealed at 1100 ℃ for 1 hour. Meanwhile, the strain caused by helium bubbles made the Si atoms diffuse out of Si layers and accumulate at the surface region. These efforts also indicate that the behaviors of helium bubbles and microstructure evolutions under He irradiation in Ti_3SiC_2 are complex, and further explorations are desirable.

In fission nuclear reactors, hydrogen (H), helium (He), and a variety of fission products are generated concurrently, leading to synergistic radiation damage in cladding materials. Regrettably, the majority of prior research has predominantly concentrated on the impact of single-ion irradiation on MAX phases. A significant knowledge gap exists in the literature concerning the effects of multi-ion irradiation. Consequently, this study seeks to elucidate the irradiation response of Ti_3SiC_2 under the synergistic effects of multi-ion irradiation, both pre- and post-annealing. Initially, 5 MeV Xe^+ ions were implanted into Ti_3SiC_2 samples to induce displacement damage and incorporate fission product xenon atoms. Subsequently, 400 keV He^+ ions were irradiated into selected Ti_3SiC_2 samples previously irradiated with Xe ions to assess the behavior of helium bubbles under the influence of Xe irradiation. Finally, 190 keV H^+ ions were irradiated into the Ti_3SiC_2 samples previously subjected to Xe+He irradiation to investigate the microstructural evolution under the synergistic effects of Xe+He+*H* ion irradiation.

2. Material and methods

Ti_3SiC_2 samples (purity: 99.9 %) were purchased from Beijing Bekei New Material Technology Corporation. The chemical composition and crystal structure of these samples were characterized and confirmed firstly, the results are shown in Fig. 1(a). 5 MeV Xe^{23+} ions with a fluence of 3.5×10^{15} ions/cm^2 were pre-implanted at room temperature by using the 320 kV ion implanter. Then the 400 keV He and 200 keV H ions irradiation experiments were carried out by using the NEC 400 kV ion implanter, with the fluences of 1×10^{17} ions/cm^2 and 6×10^{16} ions/cm^2

at room temperature, respectively. The direction of the ion incidence is perpendicular to the surface of the sample. Based on full damage cascades mode, the displacement threshold energies of Ti, Si and C were set as 25 eV, 15 eV and 28 eV, respectively, in the Stopping and Range of Ions in Matter (SRIM) simulation software during the calculation of irradiation parameters [12]. The density of Ti_3SiC_2 was set as 4.528 g/cm^3 in the SRIM calculations [25]. Fig. 1(c) and Fig. 1(d) display the simulation results of the depth variation of damage and the concentration of Xe, He and H atoms, which show that the peak displacement damage (approximately 14 dpa, displacement per atom), peak helium concentration (approximately 7 %) and peak hydrogen concentration (approximately 5.5 %) located at a depth of approximately 1 μm. In addition, some irradiated samples were annealed in tube furnace at 900 ℃ for 2 h with argon gas (purity: 99.999 %) protection. The experimental parameters are listed in Table 1.

The surface morphologies and microstructures of those unirradiated, irradiated, and annealing samples were characterized by scanning electron microscopy (SEM, Zeiss Gemini 460), transmission electron microscopy (TEM, FEI talos F200X), selected area electron diffraction (SAED) patterns, scanning transmission electron microscopy (STEM) with electron diffraction spectroscopy (EDS). The TEM samples, less than 100 nm thick, were prepared by using the focused ion beam (FIB, FEI Helios G4) lift-out technique. The initial lift-outs were performed by using 30 kV Ga^+ ions with a current of 9.3 nA. During the process of thinning, the energy and current of Ga^+ ions beam was progressively decreased to minimize damage to the sample surface. Final thinning was performed using 2 kV Ga^+ ion. Fig. 1(b) shows the overview image of FIB-prepared TEM sample, the irradiation direction and damage areas are marked. The nano-hardness of samples were measured by Hysitron

Table 1
The detailed experimental parameters used in this study.

Ion influence(ions/cm^2)			Annealing temperature (℃)	Annealing time (h)
Xe^+ ions	He^+ ions	H^+ ions		
3.5 × 10^{15}			900	2
3.5 × 10^{15}	1 × 10^{17}			
3.5 × 10^{15}	1 × 10^{17}	6 × 10^{16}		

Ti-980 Tribo Indenter, the indentation depth is 100 nm, which is corresponding to the damage region of the irradiated samples. In addition, 5 indentations were performed for each sample and the results were averaged over the five measurements.

In addition, the Density Functional Theory (DFT) method was used to investigate the atomistic behavior of defects in Ti_3SiC_2. The structural and energetic calculations were executed using the Vienna Ab initio Simulation Package (VASP) [26], adopting a supercell configuration of 5 × 5 × 1 unit cells of HCP-Ti_3SiC_2 (15.37×15.37×17.73 Å^3) with periodic boundary conditions (PBCs). The supercell (300 atoms) is optimized with a plane-wave energy cutoff of 400 eV and a gamma-only (1 × 1 × 1) k-points. The convergence criteria for structural optimization are set to 10^{-5} eV for total energy and 0.03 eV/Å for atomic forces. The Perdew-Burke-Ernzerhof (PBE) form of the Generalized Gradient Approximation (GGA) [27] is employed as the exchange-correlation functional. The Climbing Image Nudged Elastic Band (CI-NEB) [28] method was utilized to calculate the migration energy barriers of

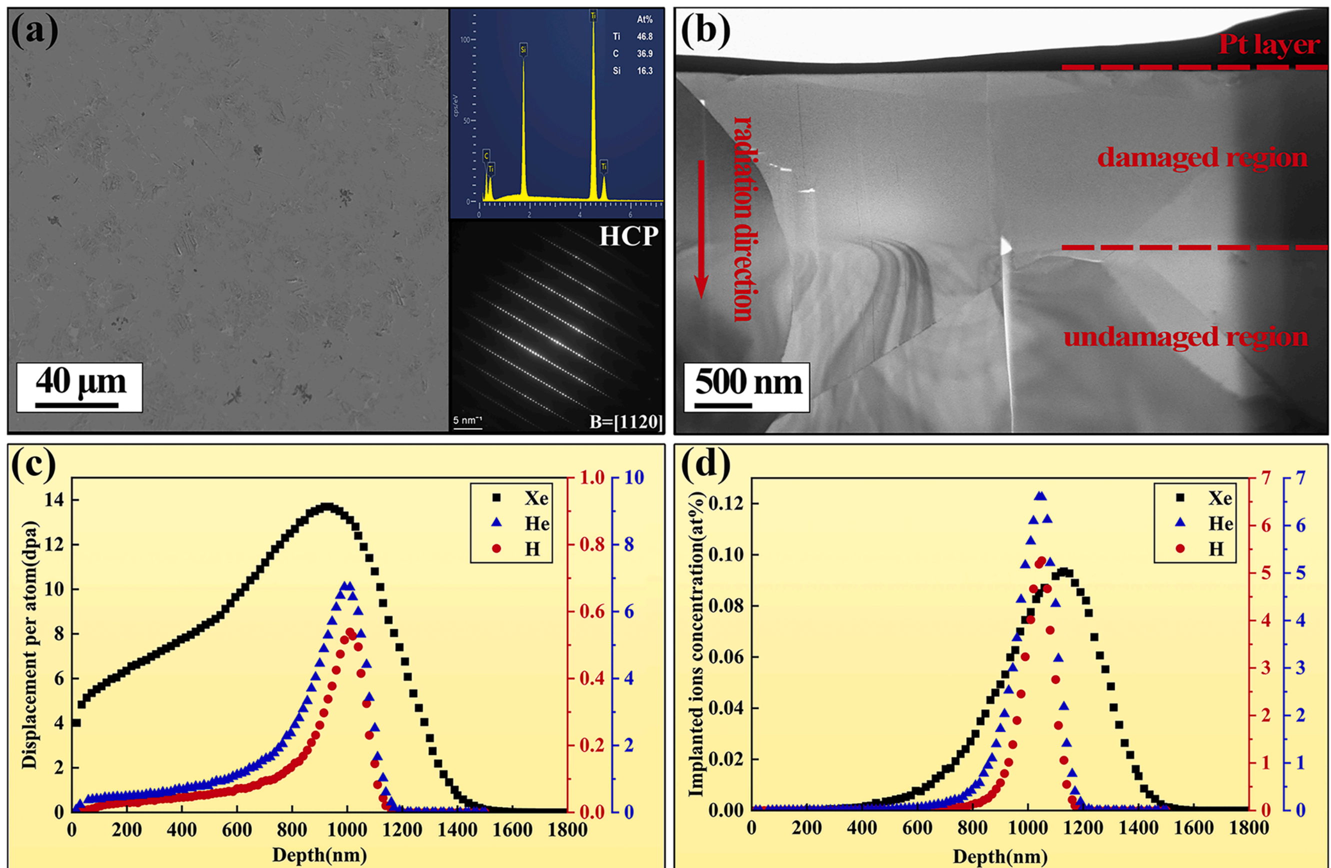

Fig. 1. (a) Surface morphology of the as-received Ti_3SiC_2 sample with its composition information (EDS) and crystal structure information (SAED pattern); (b) The overview image of FIB-prepared TEM sample; (c) the results variation of dpa (induced by Xe, He and H) in the irradiated Ti_3SiC_2; (d) the variation results of implanted atom concentrations (Xe, He and H) in the irradiated Ti3SiC2. These results are calculated by SRIM 2013 software with full damage cascades mode.

defects. The defect formation energy is calculated as $E_f = E_\alpha - E_{pft} + \sum_i n_i\mu_i$, where E_α is the total energy of the crystal with a defect α, E_{pft} the total energy of the perfect crystal (without defects), n_i the number of atoms of type i involved in the defect, and μ_i the chemical potential of atom type i. The binding energy of two defects ($\alpha,\ \beta$) in the supercell can be evaluated using the formula, $E_b = E_{\alpha\beta} - E_\alpha - E_\beta + E_{pft}$, where $E_{\alpha\beta}$ represents the total energy of the combined defect $\alpha\beta$, and E_α and E_β represent the total energy of the isolated defect α and β, respectively. Furthermore, a 3 × 3 × 3 supercell of TiC (12.84×12.84×12.84 Å^3) containing 216 atoms was employed to compute the energy associated with Si interstitial behavior within TiC. The simulation parameters for TiC were consistent with those used for Ti_3SiC_2. The box sizes for both Ti_3SiC_2 and TiC are validated to be large enough for energy convergency and avoiding image interaction between defects under PBCs.

3. Results

High-resolution TEM images (Fig. 2(a-c)) reveal the presence of defect clusters at the peak damage regions in samples irradiated with Xe ions, Xe+He ions, and Xe+He+H ions. In comparison with the sample irradiated solely with Xe ions, the defect clusters in the Xe+He irradiated sample exhibited a greater number density and size. Conversely, upon comparing Fig. 2(c) with Fig. 2(b), the number density and size of defect clusters were marginally reduced following the implantation of hydrogen ions, suggesting that hydrogen ions impede the growth of defect clusters in Ti_3SiC_2. The SAED pattern in Fig. 2(a) indicates that Ti_3SiC_2 retains its pristine HCP structure after irradiation with single Xe ions. However, upon the introduction of He and H ions, Ti_3SiC_2 undergoes a structural transformation from HCP to face-centered cubic (FCC), as evidenced by the SAED patterns in Fig. 2(b) and 2(c). Following annealing at 900 °C for 2 h, the damaged regions within the three types of irradiated Ti_3SiC_2 samples exhibited varying degrees of recrystallization recovery. In the case of the Xe+He and Xe+He+H ions irradiated samples, the majority of the irradiated regions, which had adopted an FCC structure, reverted to their original HCP structure post annealing, as demonstrated by the SAED patterns in Fig. 2(e) and 2(f). Concurrently, the annealing process resulted in the formation of a minor quantity of stacking faults, amorphous regions, and helium bubbles. Additionally, FCC phases were observed within the recrystallized Ti_3SiC_2 grains, as depicted in Fig. 2(c), suggesting that some FCC phases remained unreverted to the HCP structure upon annealing. Conversely, the SAED pattern reveals that the damaged region in the Ti_3SiC_2 sample irradiated with single Xe ions transitioned to an FCC structure after annealing at 900 °C for 2 h, and the associated HRTEM image (Fig. 2(d)) demonstrates that the crystallinity remains significantly compromised.

Fig. 3(a), (d), and (g) present overview (ov) TEM images of the three irradiated Ti_3SiC_2 samples post-annealing at 900 °C for 2 h, illustrating the internal formation of precipitates and bubbles. The remaining images in Fig. 3 correspond to underfocus (uf) and overfocus (of) TEM micrographs of irradiation-induced bubbles in the peak damage regions. The peak concentration regions of xenon and helium bubbles are situated at a depth of approximately 1000 nm, aligning well with SRIM calculations. In the sample irradiated with Xe ions, the Xe bubbles are uniformly distributed within the damage region, as depicted in Fig. 3(a)-(c), with an average diameter of approximately 2 nm. Following the introduction of He ions, Fig. 3(d)-(f) demonstrate an increase in the average bubble size and a decrease in their number density, with some helium bubbles reaching up to ~15 nm in size. In contrast to the Xe+He

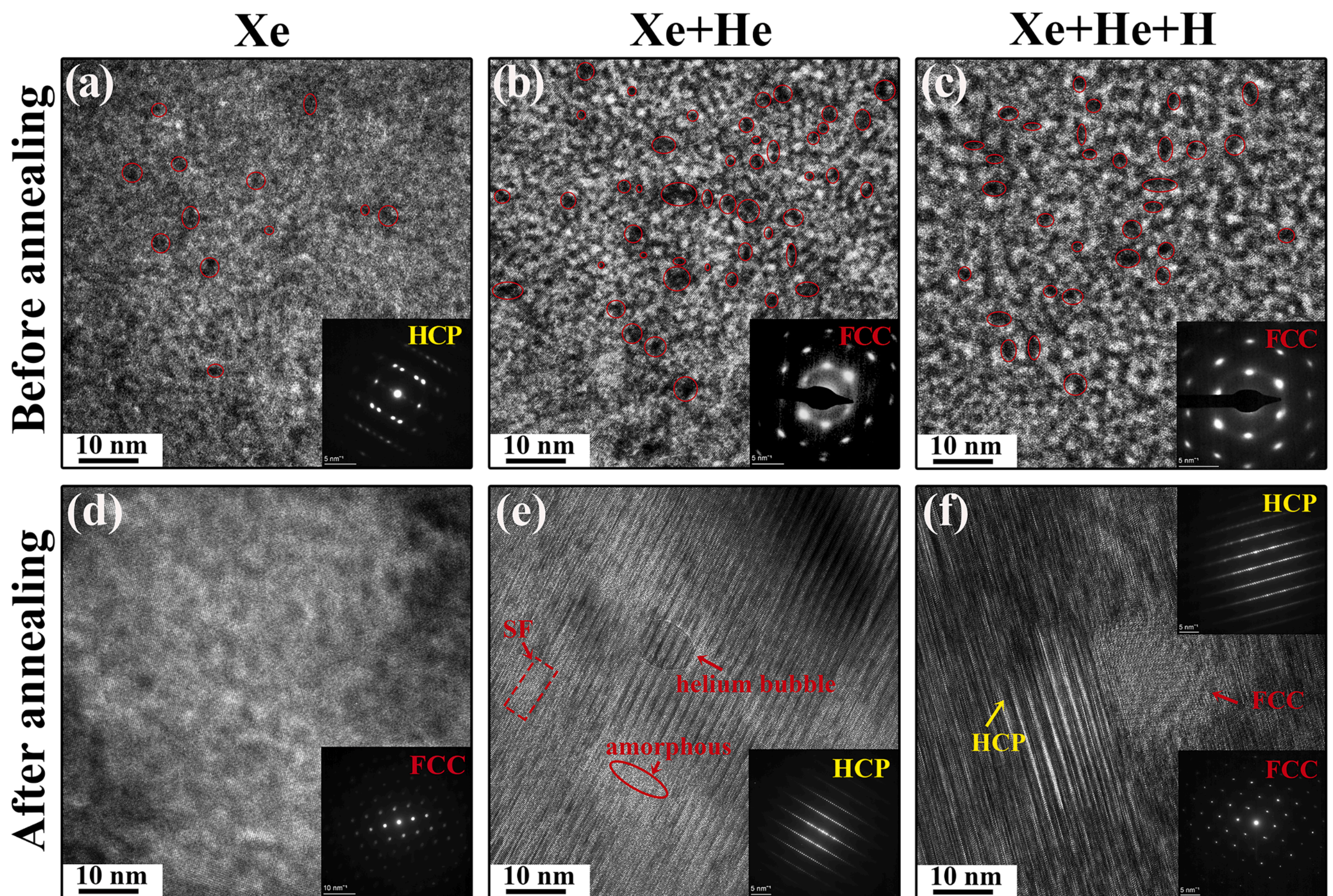

Fig. 2. The HRTEM images of the microstructure at the peak damage regions in the irradiated samples before and after annealing: (a) Xe ions; (b) Xe+He ions; (c) Xe+He+H ions; (d) Xe ions, 900 ℃, 2 h; (e) Xe+He ions, 900 ℃, 2 h; (f) Xe+He+H ions, 900 ℃, 2 h.

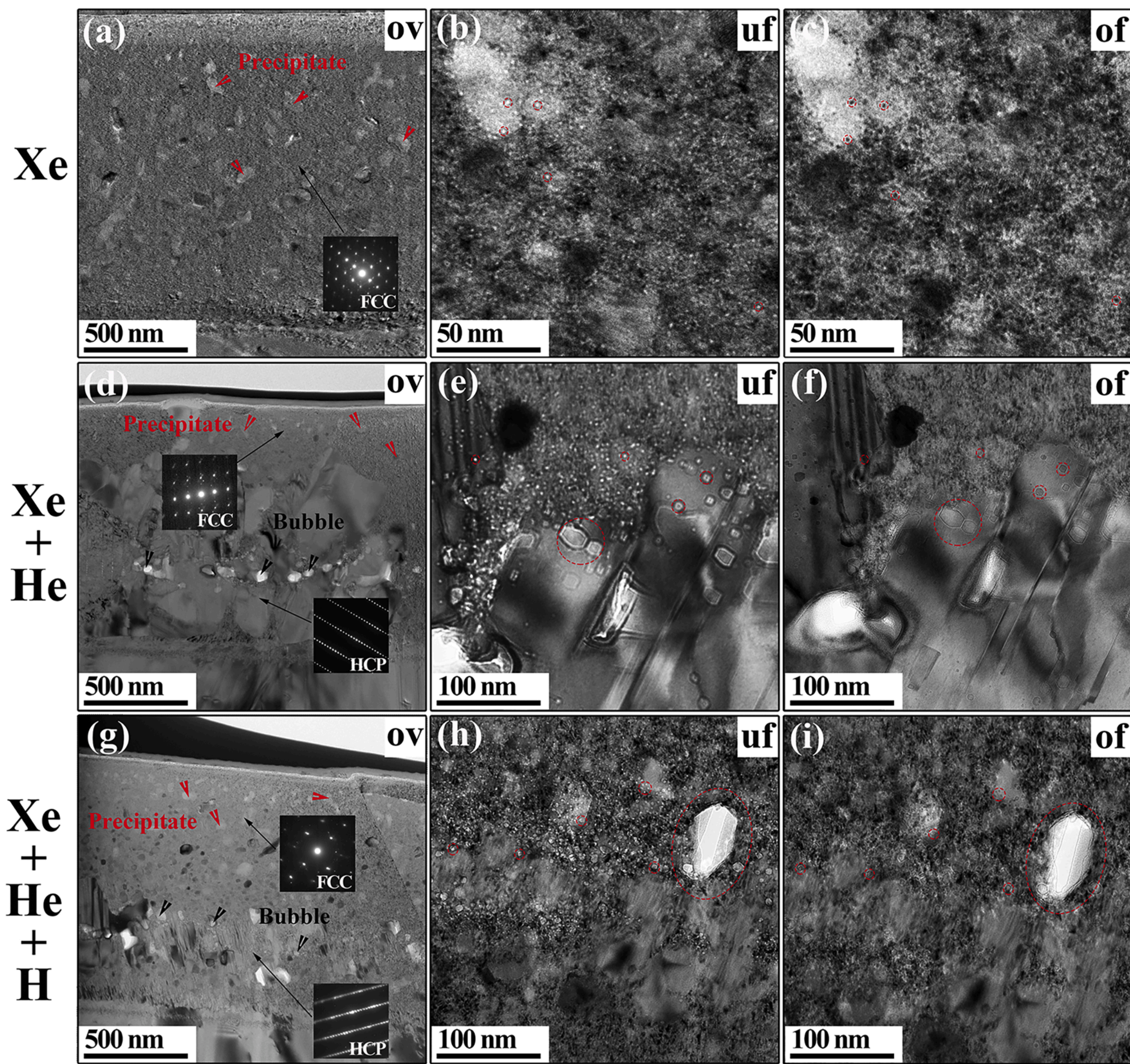

Fig. 3. The TEM images showing the irradiation induced bubbles in the peak damage regions inside the irradiated Ti_3SiC_2 samples after annealing at 900 ℃ for 2 h: (a)-(c) Xe ions irradiation; (d)-(f) Xe+He ions irradiation; (g)-(i) Xe+He+*H* ions irradiation.

irradiated samples, the addition of hydrogen ions resulted in a slight decrease in the average bubble size and an increase in their density. Nonetheless, the presence of hydrogen ions in the Xe+He+*H* irradiated samples, as evidenced by Fig. 3(h)-(i), led to the formation of several oversized bubbles, suggesting that implanted hydrogen ions promote the growth of helium bubbles during annealing. The detailed number density and size of bubbles under different irradiation conditions are given in Fig. 4.

EDX mapping results prove that all element atoms distribute uniformly in the damaged regions in these three irradiated Ti_3SiC_2 samples and no secondary phase were observed, as shown in Fig. 5(a)-(c). After annealing at 900 ℃ for 2 h, amounts of Si enrichment precipitates can be obviously observed in these irradiated samples, as shown in Fig. 5(d)-(f). The Si enrichment regions inside the Xe, Xe+He, Xe+He+*H* ions irradiated Ti_3SiC_2 samples are mainly located at the depth from 200~1500 nm, 100~500 nm and 200~1000 nm, respectively. Meanwhile, a content comparison of the Si enrichment precipitate (*P*, considering the size and density of the precipitates) in these annealed samples is: $P_{Xe} > P_{Xe+He+H} > P_{Xe+He}$. The EDX mappings and HADDF image of a rich Si area are shown in Fig. 6(a); and the corresponding HRTEM image, SAED pattern (obtained by Fourier transform) and element composition ratio of a Si enrichment precipitate marked in Fig. 6(a) are shown in Fig. 6(b), which indicate that the lattice structure of these rich Si clusters is FCC structure, and there still exists near 37 % Ti atoms. Interestingly, a band-like aggregation area of silicon atoms that parallel to the incidence direction of the ion beam was observed in a TiC grain, and it can be clearly observed from the Fig. 7 that these Si atomic clusters migrated together with the small-sized bubbles, which indicates that the interlayer gaps of the (110) planes of TiC can be served as a migration channel for the Si-He pairs.

Fig. 8 shows the nano-hardness results of the irradiated and unirradiated Ti_3SiC_2 samples before and after annealing. Compared with the unirradiated samples, the irradiated samples show a significant increase in nano-hardness, from 13.03 GPa to 20.47 Gpa. And as the subsequent incidence of He and H ions, the hardness had a slightly increase: H_{Xe} (20.47 Gpa)<H_{Xe+He} (21.57 Gpa)<$H_{Xe+He+H}$ (22.22 Gpa). The similarity in hardness magnitude under the three different irradiation conditions suggests that the implantation of He and H ions has a slight impact on the hardness of the Ti_3SiC_2 in this work. After annealing at 900 ℃ for 2 h, the nano-hardness of these irradiated samples reduced prominently. The decrease in hardness of irradiated samples after annealing is often attributed to defects recovery, but the hardness of the unirradiated samples also decreased after annealing, which is due to the release of residual stress during the annealing process. After annealing, the hardness values of these three samples at the irradiation damage region are: H_{Xe} (9.53 Gpa)<H_{Xe+He} (13.62 Gpa)<$H_{Xe+He+H}$ (15.30 Gpa). In addition,

Fig. 4. The size distribution of bubbles detected in the irradiated samples after annealing at 900 ℃ for 2 h: (a) Xe ions; (b) Xe+He ions; (c) Xe+He+*H* ions. And the number densities of bubbles were summarized in (d).

it can be seen that the hardness results of the damage areas of the annealed sample irradiated with Xe ions are approximately the same as the unirradiated sample, while the hardness of the damage regions of the Xe+He and Xe+He+*H* ions irradiated samples are significantly larger than that of the Xe ions irradiated samples after annealing, which is related to the distribution of Si-rich precipitates/He bubbles and the crystal structure of the materials.

4. Discussion

4.1. Microstructure evolution and phase transformation

Irradiation-induced damage was clearly observed in these three kinds of irradiated Ti_3SiC_2 samples, such as black spots, amorphization, structure transformation and so on. Under single Xe ions irradiation, although Ti_3SiC_2 still maintained initial crystal structure, it was not perfectly ordered; the diffraction rings and the deformation of diffraction spots in the SAED pattern indicate the occurrence of partial amorphization and disorder. When Ti_3SiC_2 samples were irradiated with Xe+He and Xe+He+*H* ions, the structure transformed from HCP to FCC structure. As convention, displacement per atom (dpa) is used to quantify the damage induced by irradiation. Shen [13] proposed that the structure of Ti_3SiC_2 remained unchanged as the damage up to 11.7 dpa (Xe ions irradiation) at room temperature, but when the damage was increased up to 58.5 dpa, the Ti_3SiC_2 sample transformed to FCC structure. This phenomenon indicates that the occurrence of structure transformation in Ti_3SiC_2 has a threshold dpa value. It is also the reason why the Ti_3SiC_2 sample remains its initial HCP structure in this study (single Xe ions irradiation, ~14 dpa). In Xe+He and Xe+He+*H* ions irradiation conditions, the extra implanted He ions can be combined with the vacancies induced by the Xe ions to form bubbles or cavities, which can inhibit the recombination of self-interstitial atoms (SIA) and vacancy defects, and lead to further damage [29]. On the other hand, point defects can be formed at the early stage of irradiation and then accumulate into clusters and stacking faults. Si interstitials can migrate along the Si layers from 2b sites to 2d sites to form the HCP-β-Ti_3SiC_2; with the increase of dpa, the cation and anion sites undergo disordering leading to the formation of HCP-γ-Ti_3SiC_2 phase. As the dose is up to a higher level (~14 dpa), the stacking faults induced by irradiation trigger the HCP-γ-Ti_3SiC_2 to the solid solution FCC-$(Ti_3Si)C_2$ phase [17], and the formation of stacking faults can be described by the following reaction:

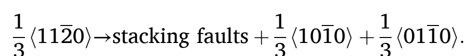

$$\frac{1}{3}\langle 11\bar{2}0\rangle \rightarrow \text{stacking faults} + \frac{1}{3}\langle 10\bar{1}0\rangle + \frac{1}{3}\langle 01\bar{1}0\rangle.$$

During the 900 ℃ annealing process, as the atomic kinetic energy increased, the irradiation-induced defects and damage were easier to be annihilated and recovered. Zinkle [30] proposed that the defects recovery can be divided into five stages at high temperature. As the temperature rises to between Stage I and Stage III, the self-interstitial

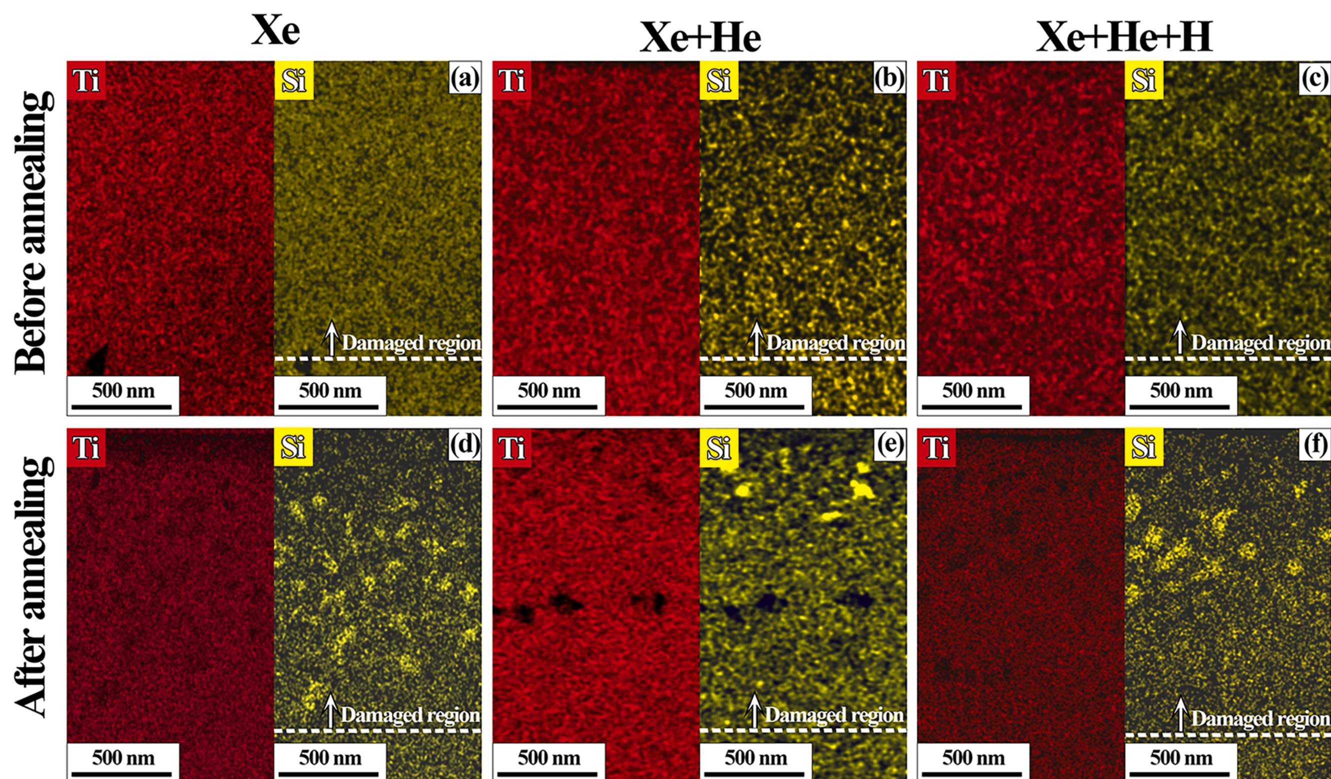

Fig. 5. EDX mapping results of the damage regions inside the ions irradiated Ti_3SiC_2 samples before and after annealing: (a) and (d) Xe ions irradiation; (b) and (e) Xe+He ions irradiation; (c) and (f) Xe+He+*H* ions irradiation.

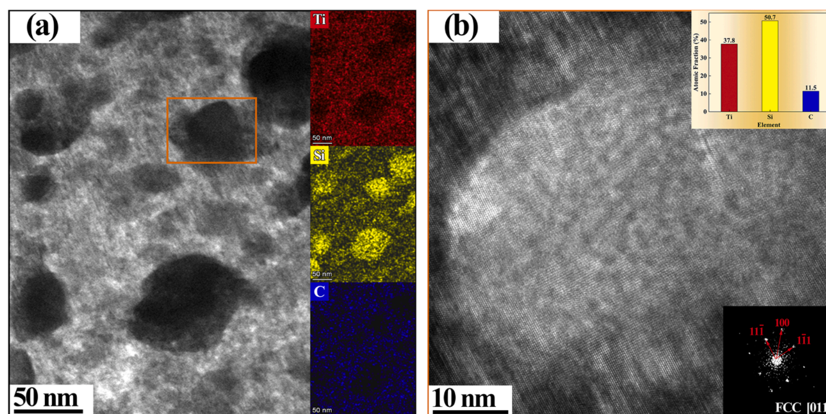

Fig. 6. (a) The HADDF image and EDX mapping results of a rich Si area; (b) The HRTEM image, SAED pattern and the EDX elemental composition ratio of the Si-rich cluster marked in (a).

atoms (SIA) and some SIA clusters have sufficient mobility to migrate and recombine with vacancy clusters and decrease the residual defects. The efficiency of recombination can be promoted with the increase of temperature. Therefore, after annealing at 900 ℃ for 2 h, most damage regions of the Xe+He and Xe+He+*H* ions irradiated samples in the damage peak band transformed back to the pristine HCP structure. However, several stacking faults, partial amorphization and partial FCC phase can also be observed in Xe+He and Xe+He+*H* ions irradiated samples after annealing. During the annealing process, firstly, the implanted He ions could greatly reduce the mechanical strength of Ti_3SiC_2 and helium atoms prefered to occupy the Si-layers in Ti_3SiC_2, leading a sharp decline in theoretical fracture stress of helium atoms occupying positions [31]; secondly, helium atoms had sufficient mobility to move from Si adjacent sites to vacancies and gathered to form larger bubbles, which generated stress around the damage areas to result in the HCP→FCC phase transformation [25], which is the reason that there are still partial FCC phases exist in the recovered HCP Ti_3SiC_2 grain, as indicated in Fig. 2(f).

Conversely, quite different from the Xe+He and Xe+He+*H* ions irradiation conditions, the HCP→FCC phase transformation occurred in the single Xe ions irradiated Ti_3SiC_2 sample after annealing at 900 ℃ for 2 h. The Xe ions, as gaseous ions, have the functions similar to the He ion in materials, leading to the formation of Xe bubbles and irradiation damage. Owing to the larger atomic mass and atomic radius, it is more difficult for Xe atoms to migrate and accumulate in the Ti_3SiC_2 than He atoms. Emmerlich [32] pointed out that Ti_3SiC_2 was very stable during annealing at temperatures up to ~1000 ℃ for 25 h. Therefore, during the 900 ℃ annealing process in this work, Ti_3SiC_2 did not spontaneously

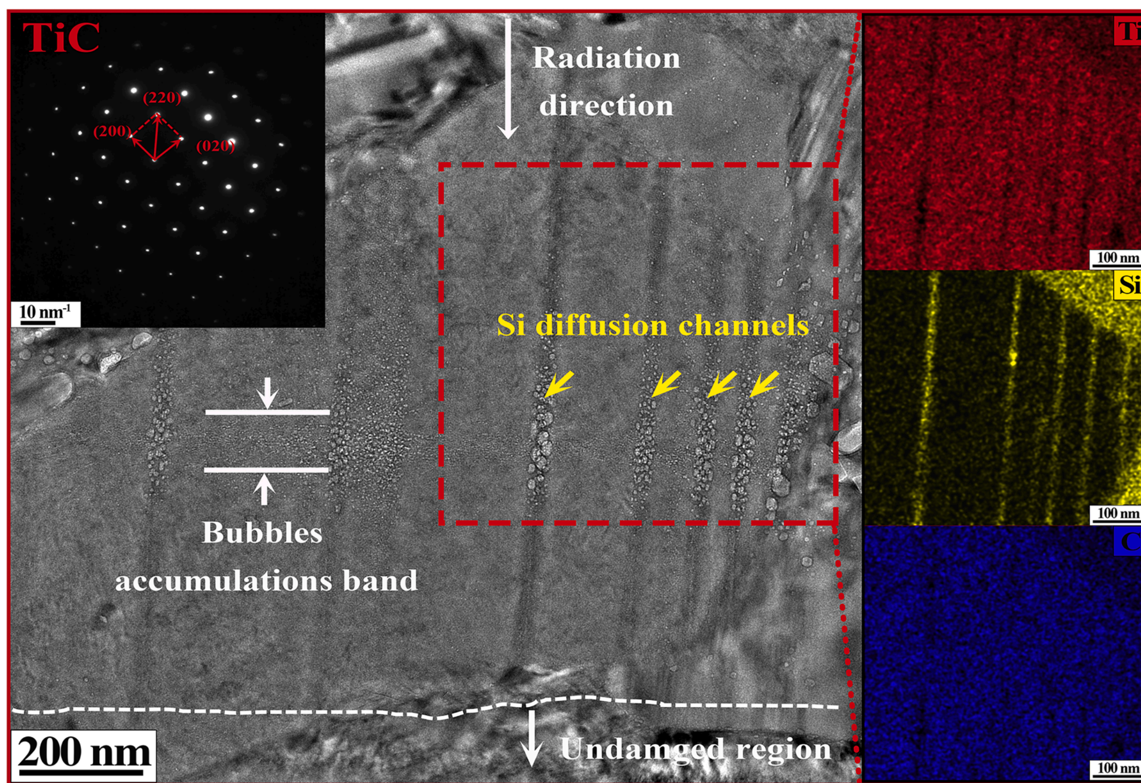

Fig. 7. The TEM image, EDX mapping results and SAED pattern of a TiC grain region with the Si diffusion channels.

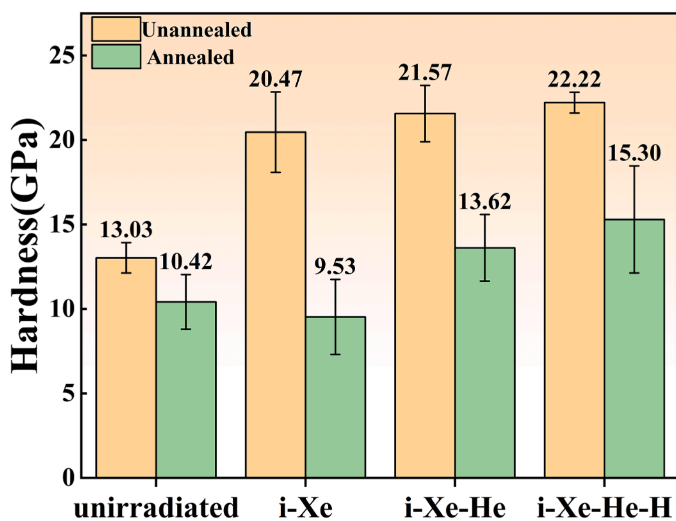

Fig. 8. Nano-hardness of irradiated and unirradiated Ti_3SiC_2 samples before and after annealing.

decomposed into TiC. However, due to the introduction of Xe ions and irradiation damage, Xe atoms could accumulate to form small Xe bubbles during annealing process, which could capture the Si interstitial atoms that near the Xe bubbles to form rich-Si clusters pinned in the damage regions, as seen in Figs. 3(a) and 5(d), which resulted in that the Si interstitial atoms were not able to return back to initial lattice sites. Thus, due to the pinning effect of Xe bubbles for the Si interstitials, the phase transformation recovery of FCC-$(Ti_3Si)C_2$ into HCP-Ti_3SiC_2 was hindered in the Xe ions irradiated Ti_3SiC_2 sample during the 900 ℃ annealing process.

4.2. Xenon and helium bubbles

Most of previous works researched the helium bubbles evolution in Ti_3SiC_2 under the single He ions irradiation. Some studies showed that the average diameter of helium bubbles grew up to 15 nm after annealing at 750 ℃ for 2 h [25]. While in this work, in Xe+He irradiation condition, the distributions of bubbles size are mainly between 4 nm and 8 nm, which shows that the helium bubbles size is slightly smaller than that in the single He irradiation condition. The difference in mean size of the irradiation-induced bubbles can be contributed to distinction of the defect reactions and vacancy supply [33]. The irradiation damage induced by pre-implanted Xe ions reached ~14 dpa in the peak helium atoms concentration areas (at the depth of ~1000 nm), including sufficient interstitial atoms and vacancies. Besides, Xe atoms accumulated to form small Xe bubbles that could trap subsequent implanted helium atoms. When He ions were implanted into Ti_3SiC_2, He clusters and He-vacancy complexes were formed and the high annealing temperature increased the mobility rate of He atoms. The stable defects like xenon bubbles, stacking faults, vacancy clusters, can capture helium atoms and could supply more nucleated sites for helium atoms to grow into large helium bubbles at the peak damage region during the annealing process [34]. Under the Xe+He+*H* ions irradiation, as the binding ability of hydrogen clusters and defects induced by the H ions irradiation is much weaker than that of He ions, those defects and incident H atoms were more likely to be trapped by the pre-formed helium clusters and promoted the nucleation of bubbles that fulfilled with Xe, He and H atoms at the peak damage and peak concentration (Xe, He and He atoms) areas (at the depth of ~1000 nm) during the annealing process [35]. On the other hand, besides few oversized bubbles formed in the peak concentration depth regions, for the Xe+He and Xe+He+*H* ions irradiated Ti_3SiC_2 samples, due to the absence of He atoms and the capture effect of Xe bubbles, a large number of small-sized He bubbles were produced on the other damaged regions during the annealing process. Therefore, the statistical results of average bubble

size within the entire irradiation damage area indicate that the mean size of bubbles in Xe+He cases is smaller than in single He cases, and the mean size of bubbles in Xe+He+*H* cases is smaller than that in Xe+He cases.

4.3. Si-rich precipitates and hardness evolutions

Compared with the unirradiated sample, the hardening phenomenon can be obviously observed after ions irradiation, as shown in Fig. 8. It is widely accepted that the hardening of materials after irradiation is owing to the defects produced during the irradiation process, which can act as barriers to pin dislocations, inhibiting the movement of dislocation lines and resulting in the increase of hardness [36]. The hardness results of these three irradiated Ti_3SiC_2 samples before annealing are similar, which suggests that the effects of He (400 keV, 1×10^{17} ions/cm^2) and H ion implantation (200 keV, 6×10^{16} ions/cm^2) on the increase in hardness of Ti_3SiC_2 are minimal. During annealing the process, most of vacancies and interstitials could diffuse out of the sample surface or recombine with each other and then annihilate, which resulted in the reduction in hardness of the irradiated samples. After annealing, the hardness of the Xe ions irradiated samples decreased back to 9.54 GPa, close to the unirradiated one, and there is almost no difference in hardness between the surface damaged area (~200 nm) and the peak damaged region (~1000 nm), which is consistent well with TEM results Fig. 3(a), as the Si-rich precipitates distribute uniformly in the entire irradiation region with the FCC structure.

The hardness of the Xe+He and Xe+He+*H* ions irradiated samples are little higher than the unirradiated one after annealing, and the hardness at the 200 nm depth region is higher than that at the peak damage location (1000 nm depth), which is due to strengthen effect of the Si-rich precipitates locate at the near-surface region. In addition. According to the diffraction patterns in Fig. 3(d) and Fig. 3(g), the surface regions of Xe+He and Xe+He+*H* ions irradiated samples are not fully recovered, the unrecovered crystal structures and defects also have an impact on hardness. Meanwhile, the hardness results indicate that H atoms has little effect on the hardness of Ti_3SiC_2 material after annealing.

Some calculation results [37] illustrate that C and Si interstitials can be easily formed in Ti_3SiC_2, those interstitials can migrate rapidly in the Si layer, especially at high temperature. As the vacancies were depleted during the nucleation process of helium bubbles, helium interstitials could be absorbed by those embryonic bubbles, those bubbles could put out the self-interstitials simultaneously. Then, Si self-interstitial atoms could accumulate to evolve into small clusters or the second phase. High temperature could accelerate the process. The formation of second phase and dislocations may result in hardening. Helium atoms are preferentially captured by vacancies, as more helium atoms are trapped, helium clusters and bubbles can be formed in the Si layers in Ti_3SiC_2. Si atoms could be knocked off by the high-pressure caused by helium bubbles, forming high mobile Si interstitials [38]. Large He bubbles with high density induced extreme compression and strain on the lattice near that region. Interstitial silicon atoms located at any voids will be compressed and migrate further to low He regions [24]. According to SRIM simulation results in Fig. 1(c), the pre-implanted Xe ions could cause considerable damage (~7 dpa) near the surface region, interstitial Si atoms could migrate to those areas to absorb vacancies induced by Xe ions irradiation to form Si clusters.

4.4. DFT calculations for the defect evolutions

In this work, the first-principles calculations within Density Functional Theory frame have been performed to gain insights into the defect formation and migration in Ti_3SiC_2. The atomistic structures of Ti_3SiC_2 model of this study are displayed in Fig. 9. The most common defects during irradiation are vacancies and interstitials. For the three elements in Ti_3SiC_2, there are four types of single vacancies, namely V_C, V_{Si}, V_{Ti_a}, and V_{Ti_b}. according to their local chemical environments. There are two different Ti sites. One is between two carbon layers and the other is close to Si layers. The formation energies are 2.458, 2.677, 7.608, and 5.495 eV for V_C, V_{Si}, V_{Ti_a}, and V_{Ti_b}, respectively. The three most energy-favorable interstitial sites are I-SiC, I-SiTi and I-Ti, which are displayed in Fig. 9(e). I-SiC site is a tetrahedral site formed by 3 Si atoms and 1 carbon atom, denoted as I1. I-SiTi site is a tetrahedral site composited by 3 silicon atoms and 1 Ti atom, denoted as I2. I-Ti site is a tetrahedral site enclosed by 4 Ti atoms and denoted as I3 site.

We have investigated the formation energies of six interstitial configurations at sites I1, I2, and I3, each occupied by an atom of C, Si, Ti, H, He, or Xe. The formation energies are presented in Fig. 10. It is evident that the I1-Si configuration is the most energetically favorable, while the formation of interstitial sites for Xe is less energetically favorable. Consequently, our subsequent investigations primarily concentrate on the I1-Si interstitial.

During irradiation-induced displacement cascades, a lattice atom is displaced from its site, occupying an interstitial position within the lattice, thereby creating a vacancy at its original site. This pair, consisting of a vacancy and an interstitial, is termed a Frenkel-pair defect. We have assessed the formation energy of Si Frenkel-pair defects, selecting seven configurations based on varying interstitial-vacancy

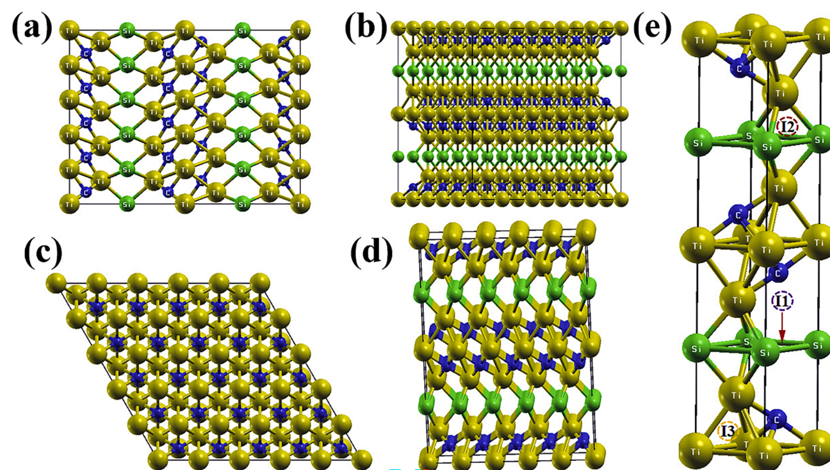

Fig. 9. Atomistic structure of Ti_3SiC_2: (a) x-side view (b) y-side view (c) z-overview, (d) tilt-view of the $5 \times 5 \times 1$ supercell (300-atom-cell). (e) the primitive unit cell (12-atom-cell) of the Ti_3SiC_2. The three interstitial sites are marked in dashed circle in (e). I1 (Dashed-purple-circle) for I-SiC; I2 (dashed-red-circle) for I-SiTi; I3 (dashed-yellow-circle) for I-Ti. The red-solid arrow points to the relaxed site of an interstitial in this work except the H or He atom.

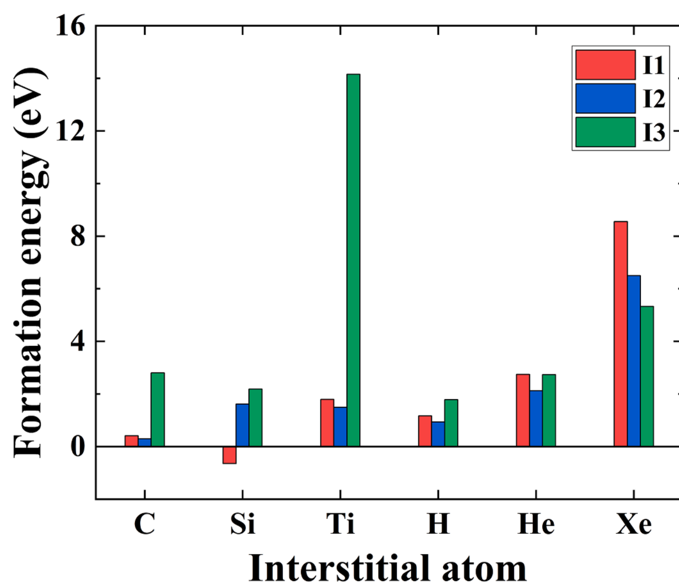

Fig. 10. Formation energies of C, Si, Ti, H, He, and Xe at interstitial sites I1, I2, I3, respectively.

separation distances, specifically 1.94, 3.63, 4.76, 6.45, 7.14, 9.34, and 10.75 Å, as depicted in Fig. 11.

In the initial four configurations, the interstitial and vacancy are located within the same Si layer plane, while the interstitials and vacancies in the latter three configurations are situated in distinct Si layer planes. The formation energy of Si Frenkel-pairs as a function of interstitial-vacancy distance is represented by the squared line in Fig. 11 (i). This curve also delineates the potential profile of the Si Frenkel-pair defect in HCP Ti_3SiC_2. At a separation of 1.94 Å, the vacancy site is positioned at the vertex of a tetrahedron. The Frenkel pair is sufficiently close for the interstitial and vacancy to recombine, resulting in a perfect lattice. The formation energy peaks at a separation of 4.76 Å. However, the potential profile exhibits a plateau at separations greater than 3.63 Å.

The vacancy serves a sink to absorb interstitials. When the vacancy has absorbed another type of interstitial, they form a small complex of Frenkel-X configuration. When X is He for example, Frenkel-He configuration equals $(V_{Si}+\text{He}) + \text{I1}_{Si}$, where vacancy at Si site has a He atom, and a Si atom is in I1 site. In ordinance with experiment, we have examined three elements, H, He, and Xe. The formation energy of Frenkel-X ($X = H$, He and Xe) as a function of the distance between the Si interstitial I1_{Si} and the substituted Si site with X are illustrated in Fig. 11.

A general trend of the formation energy of Si Frenkel-pair and Frenkel-X complex is that there is a plateau when the distance is beyond 3.63 Å. This plateau suggests a low migration energy barrier for the diffusion of the Si interstitials. The calculated value of migration energy of a Si interstitial is 0.056 eV equal to the thermal energy of 650 K, which suggest that the thermal energy can easily drive such a migration at temperature above 650 K.

In order to have atomistic insights on the properties of bubbles in the irradiation, we have investigated the energy profile of the initial nano bubbles. It is well accepted that the bubble nucleated at the vacancy sites. Therefore, we have examined the trap capability of the single vacancies of four typical vacancy sites of carbon atom lattice site, silicon atom lattice site, titanium atom lattice site a (Ti_a, titanium within two carbon layers) and titanium atom lattice site b (Ti_b, titanium close to silicon layers) for the irradiated ions (H, He and Xe).

The formation of hydrogen bubbles is a common occurrence during irradiation. Consequently, we initially assessed the trapping capacity of single vacancies across the four types. The outcomes, depicting the trapping of up to six hydrogen atoms for the four vacancy types, are presented in Fig. 12. Formation energy quantifies the energy required to create a defect, with lower values indicating a higher propensity for defect formation. A general trend observed is that formation energy increases with the number of trapped hydrogen atoms, as shown in Fig. 12(a). Titanium vacancies exhibit significantly higher formation energies compared to carbon and silicon vacancies, indicating a preference for hydrogen trapping in carbon and silicon vacancies. Binding energy reflects the binding strength of the trapped atoms, with negative values indicating favorable binding and positive values suggesting unstable binding. The binding energy profiles for hydrogen atoms ranging from two to six, within the four single vacancy sites, are depicted in Fig. 12(b). The findings indicate that a carbon vacancy can stably accommodate two hydrogen atoms, whereas a silicon vacancy can support up to five hydrogen atoms. Ti_a and Ti_b vacancy is able to trap three and four hydrogens, respectively. The binding energy analysis suggest that the 5-atom hydrogen bubbles are likely to nucleated at a silicon vacancy site. Noted that none of H atoms forms molecular in the vacancies. The separation distances of H atoms range from 1.5 to 3.5 Å in all calculated cases compared to 0.75 Å for the H_2 molecular in vacuum.

In the same way, the formation of helium bubbles embryos was also investigated. The formation energy of up to three helium atoms in a single vacancy are displaced in Fig. 13(a). The formation energies of helium clusters are lowest in Si vacancy sites, suggesting that helium is most likely to occupy the silicon vacancies. The corresponding binding energies are illustrated in Fig. 13(b). All the positive binding energy suggest that the Helium bubbles are unlikely form in a single vacancy. We have further studied the formation of xenon bubbles embryos. The formation energy of up to two xenon atoms in a single vacancy are displaced in Fig. 13(c). The formation energies of single xenon are lowest in Si vacancy sites, suggesting that xenon is most likely to occupy the silicon vacancies. The corresponding binding energies are illustrated in Fig. 13(d). All the positive binding energy suggest that the xenon bubbles are unlikely form in a single vacancy.

Besides single species, we have examined the formation of complex small clusters, including two or more element atoms. The formation energy of He-H, He-H-H, He-H-He in a single vacancy are displaced in Fig. 14(a). For the VSi-He-H configuration for example, one He and one H occupies the silicon vacancy site. Its formation energy is 8.773 eV, higher than that in carbon vacancy site (6.064 eV) and Ti_b vacancy site (7.748 eV). Then further addition of one H atom (thus He-H-H configuration) and one He atom (thus He-H-He configuration) are considered. It is interesting to find that three-atom cluster of He-H-H on the silicon vacancy site has the lowest formation energy of 4.562 eV among all the examined configurations. The binding energy analysis Fig. 14(b) reveals that the binding energy of the additional H atom is high, −5.378 eV. The negative sign just marks it is a stable binding. Comparing with Fig. 12 (b), this is clear evidence that the present of He atom in a vacancy enhanced the capture of hydrogen atoms and forming of hydrogen bubbles. The binding energy results also show that these different vacancies (C, Si, Ti_a, Ti_b) can trap He-H-H clusters but not He-H-He clusters. Small He clusters or He bubbles is unlikely to form in the presence of enough H. This result aligns well with the experiment observation.

Subsequently, we investigated the formation of Xe-based complex clusters, such as Xe-H and Xe-H-H. Configurations involving two or more Xe atoms within a single vacancy are found to be unstable. The formation energies of Xe-H and Xe-H-H clusters on a single vacancy site are depicted in Fig. 14(c). Both clusters in silicon vacancy sites exhibit the lowest formation energies among the four single vacancy sites, with values of 6.879 eV for Xe-H and 8.193 eV for Xe-H-H configurations. Analysis of binding energy, as shown in Fig. 14(d), indicates that the addition of hydrogen is energetically unfavorable except at the Ti_b site. The formation energies for both Xe-H and Xe-H-H at the Ti_b vacancy site are 12.632 eV and 10.312 eV, respectively. The elevated formation energies of Xe-H and Xe-H-H defect clusters reduce the likelihood of

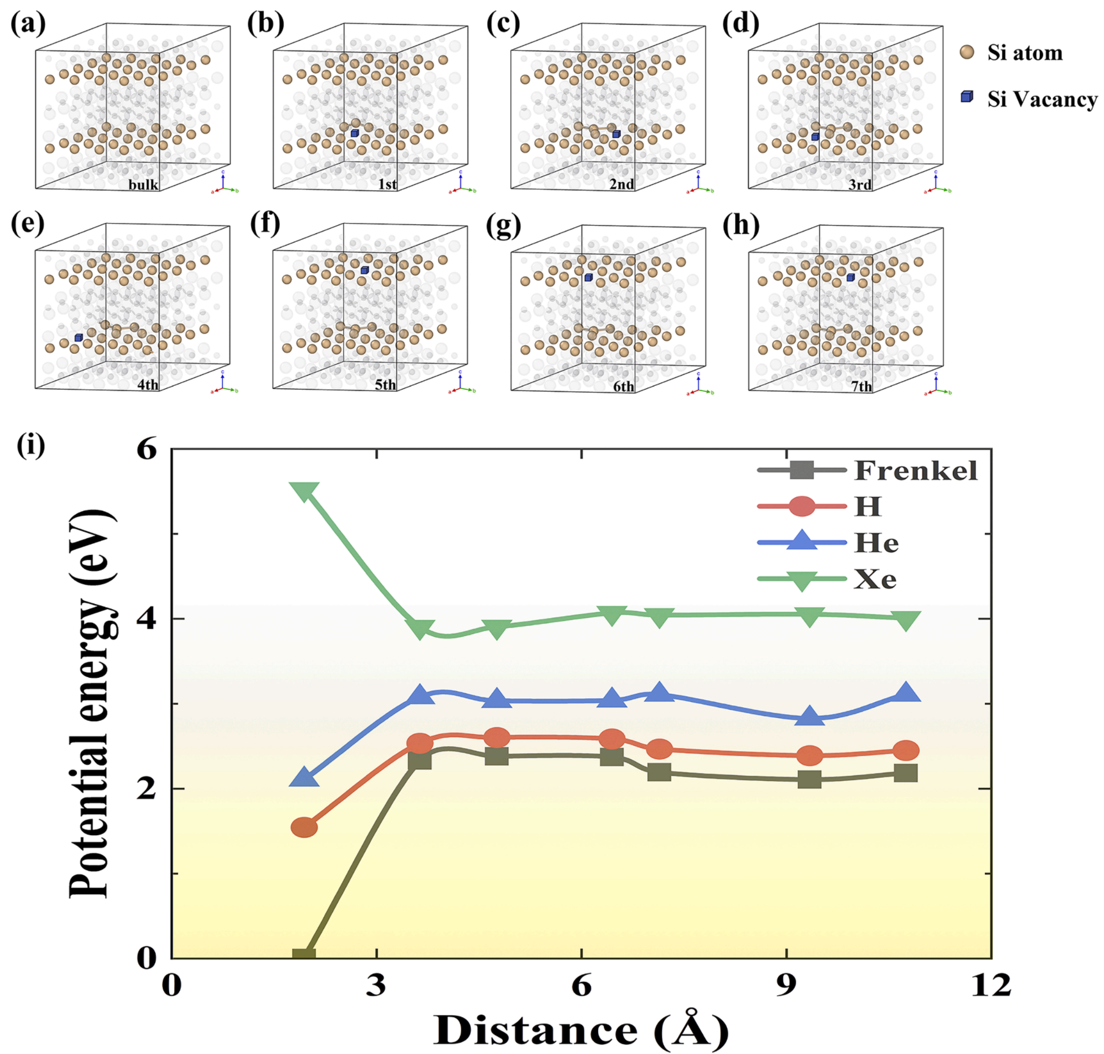

Fig. 11. (a) A layered Si atomic bulk model without defects; (b)-(h) Seven configurations of Si Frenkel-pair defects with the increased distance of the interstitial-vacancy separation in Ti_3SiC_2; (i) The formation energy of Si Frenkel-pair defect (squared line), Si Frenkel-H (circle line), Si Frenkel-He (up-triangle), and Si Frenkel-Xe (down-triangle) as a function of the interstitial-vacancy distance for seven configurations of Frenkel-X for each species.

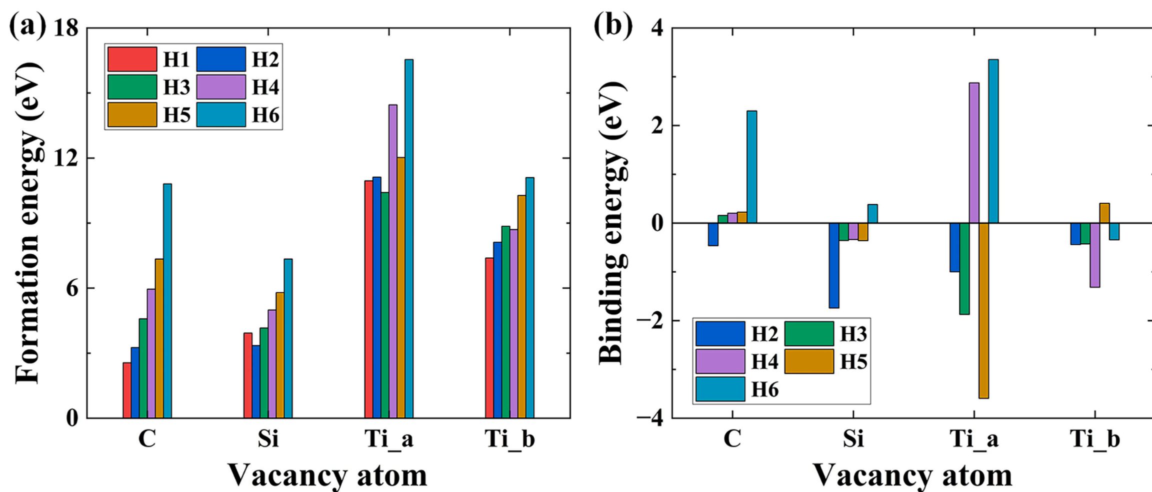

Fig. 12. (a) The formation energy and (b) binding energies as a function of the number of hydrogen atom trapped in the single vacancy of C, Si, Ti_a, and Ti_b.

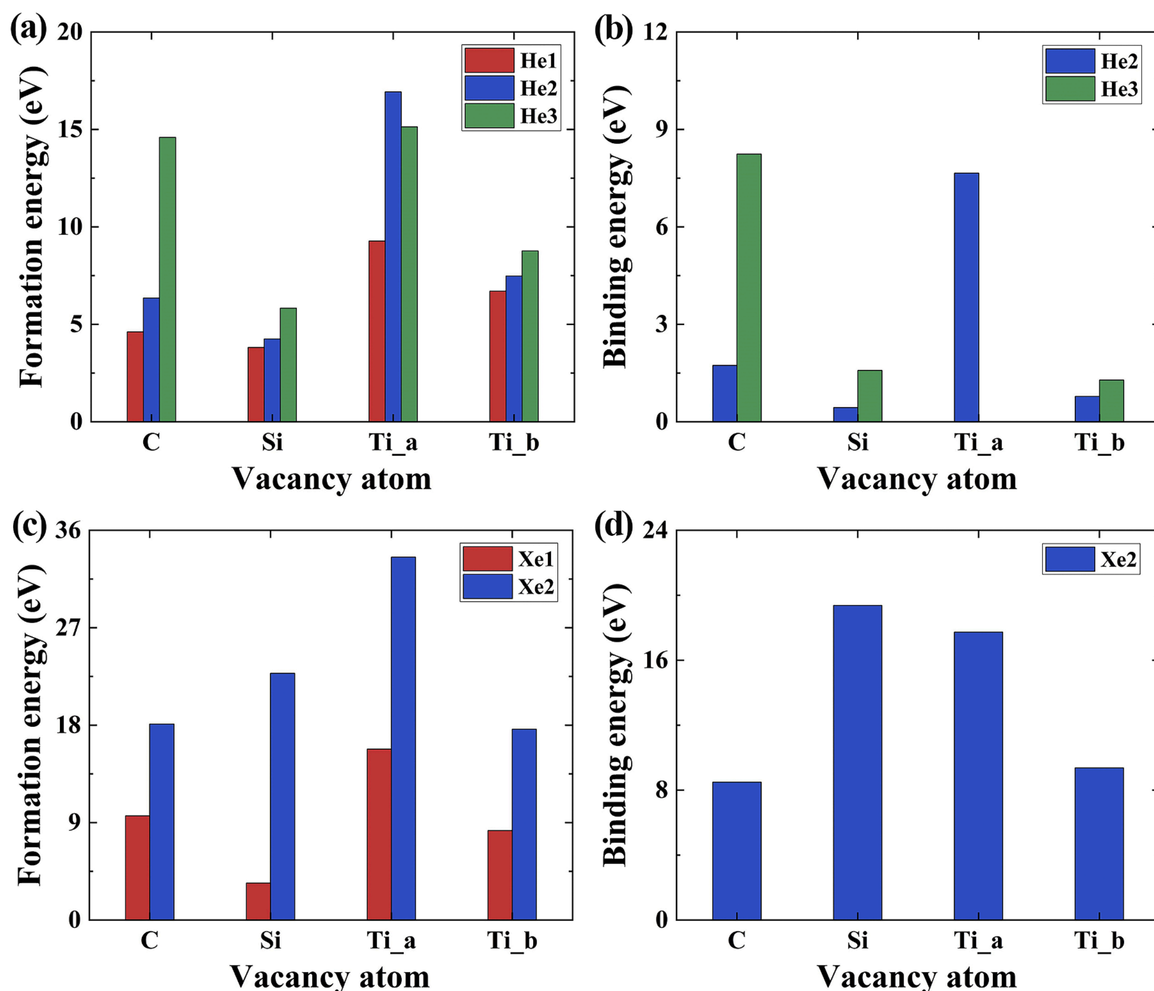

Fig. 13. (a) The formation energy and (b) binding energies as a function of the number of helium atoms trapped in the single vacancy of C, Si, Ti_a, and Ti_b; (c) The formation energy and (d) binding energies as a function of the number of Xeon atoms trapped in the single vacancy of C, Si, Ti_a, and Ti_b.

their occurrence on lattice sites.

It is worth noting that the formation energy and migration energy of a defect synergistically determines the mass transport of the defect during the annealing and nucleation process. A difference in formation energy does not have much impact on the population of the initially generated defects during collision cascade. However, the formation energy determines the thermal equilibrium states of defects during the thermal nucleation and annealing processes. Meanwhile, the migration is thermodynamically driven. The speed of migration of defect is proportional to the exponential factor of the migration energy difference. Therefore, the migration energy is critical for the transport of the defects during the annealing process, which controls specific physical processes related to the time evolution.

Based on our DFT calculations, the segregation and bubble growth process in Ti_3SiC_2 under different successive implantation could be addressed from the migration of Si interstitials. Under solely Xe irradiation, the Si Frenkel pairs are easily to form since the energy of separated Si interstitial and Xe-vacancy complex is much lower than that of a Xe interstitial in the perfect lattice (see the energy profile in Fig. 11). Then the Si interstitial could escape the vicinity of the vacancy quickly under thermal activation because of extreme low migration energy [38]. The massive Si interstitials segregated together and formed clusters locally in the materials. As Xe+He implantation, compared with solely Xe irradiation, the He atoms enhanced the recombination of Si Frenkel pairs (Fig. 11). He could segregate into the vacancy at the speed of the same order of magnitude as Si interstitial [22] and further formed bubbles, which trapped Xe and Si interstitials and reduced the Si cluster in the material. Only part of the Si interstitials could escape from the peak depth of Xe+He region into the subsurface. When H ion was added into the flux, few oversized bubbles formed in the peak concentration (He and H atoms) depth regions (~1000 nm). Based on the binding energy shown in Fig. 14(b), the He atoms preferred to be surrounded by H atoms in the voids. The diffusion and segregation of He atoms was decreased by the H atoms. Thus, extra Si interstitials could segregate into clusters under less He traps. Experimentally, compared with the Xe+He ions irradiated sample, the degree of recrystallization of Xe+He+*H* ions irradiated sample is lower, and the dispersion of its precipitates is also higher, which is consist with some research results that the implanted hydrogen ions play a negative role on the interlayer bonding strength via leading to electron localization on Si atom and deteriorating the interatomic bonding between Si and Ti atom [39].

To elucidate the formation mechanism of the strip-like Si clusters observed in TiC grains post-irradiation (Fig. 7), we quantified the energy and migration barriers for Si in TiC (Table 2). Drawing upon computational outcomes and the inherent properties of Ti_3SiC_2 and TiC, we propose a plausible formation mechanism (Fig. 15(a)). The details are follows. (1) Prior to irradiation, TiC grains contained negligible Si atoms, and consequently, Si primarily originates from Ti_3SiC_2. As previously noted, Si interstitials are readily generated in Ti_3SiC_2 during irradiation, with a low migration barrier of 0.056 eV, facilitating rapid segregation of Si along the basal plane of the HCP lattice to the Ti_3SiC_2-TiC grain interfaces. (2) Si readily forms clusters within TiC, attributed

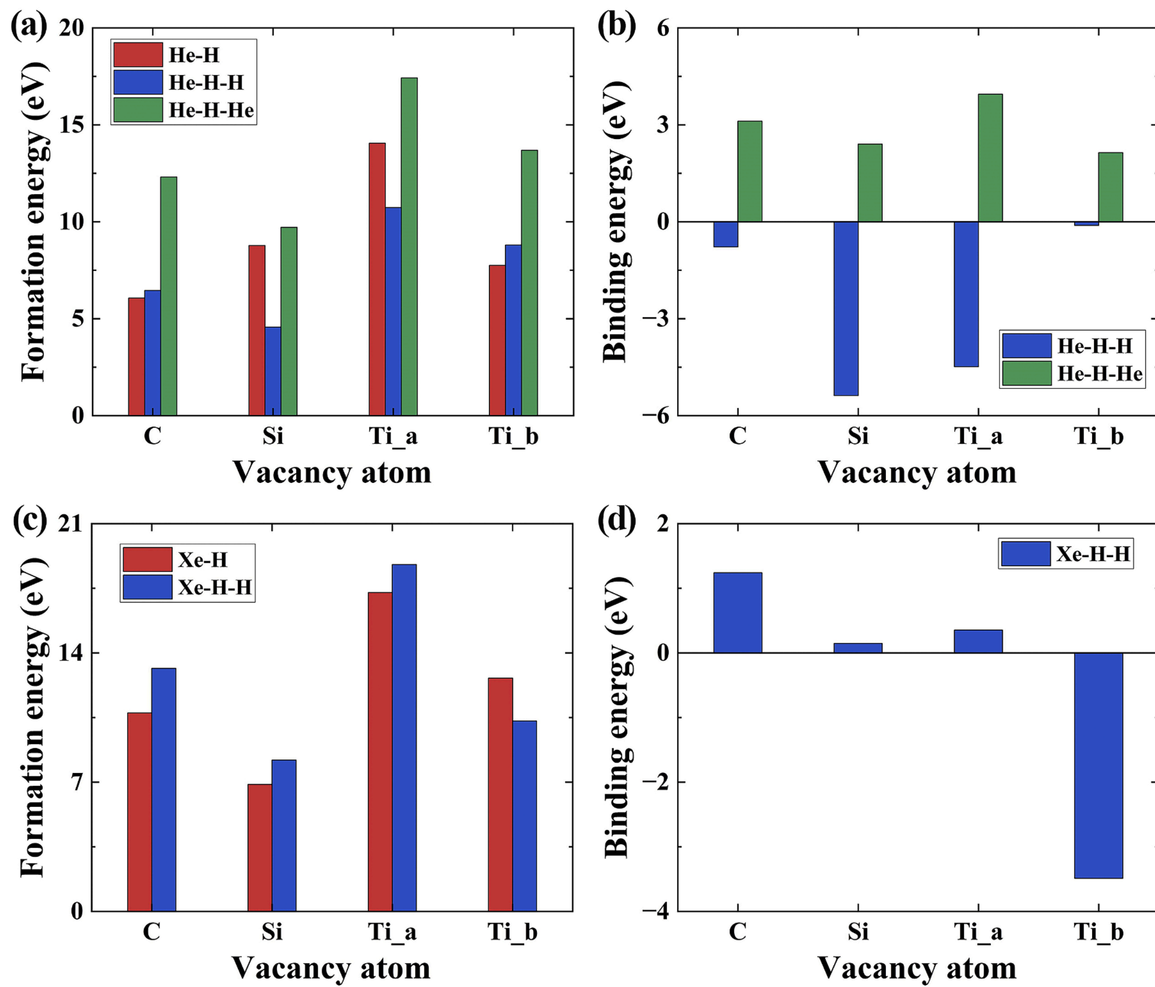

Fig. 14. Formation (a) and binding energies (b) of different atomic clusters (He-H, He-H-H, He-H-He) at different vacancies (C, Si, Ti_a, Ti_b); Formation energies (c) and binding energies (d) of different atomic clusters (Xe-H, Xe-H-H) at different vacancies (C, Si, Ti_a, Ti_b).

to the negative binding energies of Si interstitial and substitutional clusters. Additionally, Xe and He implantations induce the formation of C vacancies in TiC, offering energetically favorable sites for Si. Consequently, at the interface, the substantial presence of Si atoms induces localized anisotropic stresses within the TiC grains. (3) At the interface, the growth of Si clusters induces local stress in TiC, leading to the emission of dislocations or loops, thereby creating space for additional Si atom trapping. Si atoms continue to accumulate until a stress threshold is reached, at which point TiC emits dislocations or loops once more, facilitating continuous growth of Si clusters within the TiC grains. Additionally, the dominant slip system in TiC is {110}<110> [40], which is consistent with the experimentally observed orientation of Si strip-like clusters (<110>). These processes primarily occur under Xe+He irradiation. Helium bubbles also grow within TiC and concurrently promote the generation of dislocation loops in TiC.

Additionally, as observed in Fig. 7, there is a significant but small-scale distribution of Si atoms within TiC. Apart from the originally present in TiC grains and the possibility of Si being kicked from Ti_3SiC_2 due to the ion implantation. Si can permeate into the TiC grain through thermal diffusion facilitated by the presence of He atoms (#4 in Fig. 15). Based on the migration barriers for Si in bulk TiC and in the presence of He interstitial or vacancy-He complex (Table 2), we can estimate the diffusivity of Si under different conditions by using the Arrhenius's formula, $D = \nu_0 l^2 \exp\left(-\frac{E_m}{kT}\right)$ [41], where ν_0 is the attempt frequency (calculated by the Vineyard formula as 1.32×10^{13}/s from the vibration frequency mode of the Si atom [42]), l is the distance of Si atom jumping between the neighbor sites (2.14 Å, half of the TiC lattice constant calculated in this work), E_m is the corresponding migration barrier, k is the Boltzmann constant, and T is the annealing temperature taken as 1173 K from the experimental conditions. Qualitatively, the migration barrier for Si in the presence of He is taken as the average value (2.32 eV) of the migration barriers of Si in bulk TiC and near the vacancy-He complex (Table 2). The mean time for particle migration is directly proportional to the square of the migration distance and inversely proportional to the diffusivity ($\overline{\tau} \sim \frac{L^2}{2D}$ derived from Fick's laws). Here, the migration distance is assumed to be 1 μm (see Fig. 7, the thickness of the TiC grain).

Utilizing the parameters and assumptions outlined above, we estimate that Si migration from one interstitial side of the TiC boundary to the other would require approximately 4200 h during annealing. This implies that, under the experimental conditions detailed in this study, a substantial amount of Si is unlikely to enter the TiC crystal core via thermal activation spontaneously. Conversely, under He irradiation, the Si migration time is reduced to approximately 6 h, aligning with the experimental annealing duration of 2 h. It is noteworthy that the He concentration in DFT calculations is approximately 0.5 % (1/216), whereas in actual experiments, the peak concentration reaches approximately 7 % (Section 2). Consequently, we posit that the presence of He atoms enhances Si diffusivity by at least 700 times at 1173 K, enabling significant Si infiltration into the TiC grain via thermal activation within the actual experimental timeframe. Additionally, as

Table 2
Formation, binding, and migration energies (in eV) of defects in TiC. I and V represent the interstitial and vacancy defects, respectively. The most stable interstitial stie in TiC is the cubic center of the lattice. $I_{Si}I_{He}$ represent the 1NN complex of an interstitial Si and an interstitial He. S_{Si}^{C} and S_{Si}^{Ti} represent the configurations of Si substituting the C and Ti atom, respectively. S_{X}^{C} ($X = H$, He, and Xe) represent the configurations of X atom substituting the C atom, i.e. the V_C-X complex. $S^{n}{}_{Si}^{C}$ and I_{Si}^{n} represent the Si clusters containing n S_{Si}^{C} and I_{Si}, respectively. $S_X^C + I_C - I_X$ describes that an X atom kick off an C atom from the lattice into a C interstitial in TiC. M_{Si} represents the migration energy of the Si interstitial in bulk (M_{Si}^{bulk}), in SiHe cluster (M_{Si}^{He}), and in the presence of the V_C-He complex ($M_{Si}^{S_{He}^{C}}$). M_{He}^{bulk} and M_{He}^{Si} represent the migration energy of He interstitial without and with 1NN Si interstitial, respectively. The detailed configuration of Si-He cluster is shown in Fig. 15.

Formation		Binding	
I_{Ti}	7.34	$S^{2}{}_{Si}^{C}$	−0.66
I_C	2.99	$S^{3}{}_{Si}^{C}$	−2.66
I_{Si}	4.25	$S^{4}{}_{Si}^{C}$	−5.22
V_{Ti}	9.87	I_{Si}^{2}	−0.52
V_C	0.33	I_{Si}^{3}	−0.73
S_{Si}^{C}	1.38	I_{Si}^{4}	−0.50
S_{Si}^{Ti}	7.09	$I_{Si}I_{He}$	−0.73
		$I_{Si}S_{He}^{C}$	0.10
I_H	0.10	$S_H^C + I_C - I_H$	0.53
I_{He}	5.51	$S_{He}^C + I_C - I_{He}$	−0.93
I_{Xe}	21.22	$S_{Xe}^C + I_C - I_{Xe}$	−8.34
Migration			
M_{Si}^{bulk}	3.09	M_{He}^{bulk}	0.29
M_{Si}^{He}	2.60	M_{He}^{Si}	0.38
$M_{Si}^{S_{He}^{C}}$	1.60		

previously discussed, Si clusters readily segregate and grow through the emission of ⟨110⟩ dislocations or loops in TiC, resulting in the formation of stripe-like Si layers oriented along the ⟨110⟩ direction.

5. Conclusions

This study investigates the synergistic effects of Xe, He, and H ions irradiation on the microstructural evolution of Ti_3SiC_2, both pre- and post-annealing, employing a hybrid experimental and first-principles computational approach. Irradiation with single Xe ions led to amorphization and disorder in Ti_3SiC_2, yet the initial layered crystal structure was preserved. Following the implantation of He and H ions, the structure transitioned from the pristine HCP to FCC. Post-annealing, the structure of the sample irradiated with single Xe ions evolved into FCC-$(Ti_3Si)C_2$, attributed to the pinning effect of Xe bubbles on Si atoms. Conversely, in the samples irradiated with Xe+He and Xe+He+H ions, the majority of regions reverted to the HCP-Ti_3SiC_2 structure. The mean size of bubbles in these irradiated Ti_3SiC_2 samples after annealing is: $D_{Xe+He} > D_{Xe+He+H} > D_{Xe}$, which is releated with the supply of vacancies and He atoms. H atoms can reduce the surface energy of bubble nucleation and growth.

There is a significant increase in nano-hardness of the Ti_3SiC_2 samples after irradiation., while the effects of He and H ion implantation on the increase in hardness of Ti_3SiC_2 are minimal (H_{Xe} : 20.47 Gpa, H_{Xe+He}: 21.57 Gpa, $H_{Xe+He+H}$: 22.22 Gpa). However, there were significant differences in the hardness of the irradiation damage regions of these irradiated samples after annealing (H_{Xe} (9.53 Gpa)<H_{Xe+He} (13.62 Gpa)<$H_{Xe+He+H}$ (15.30 Gpa)), which is due to the distribution, size and density of the Si-rich precipitates and He bubbles that formed in the damage regions and the crystal structure of the damage regions in the materials. Thermodynamic energy calculations demonstrate that Xe atoms can spontaneously create Si Frenkel pairs, leading to the formation of numerous Si interstitial clusters. Concurrently, He atoms facilitate the recombination of Si Frenkel pairs, enabling only a limited number of Si interstitial clusters to migrate to the sample surface from the peak damage region. The addition of H atoms can augment the formation of Si precipitates by promoting He bubble nucleation.

Within TiC grains, Si atomic clusters were observed migrating in conjunction with small-sized bubbles. Additionally, a substantial number of Si atoms segregate to the interfaces between Ti_3SiC_2 and TiC grains. DFT calculations suggest that strip-like Si clusters are formed, oriented along the ⟨110⟩ direction, through the emission of ⟨110⟩ dislocation loops within TiC. Moreover, He significantly enhances Si interstitial diffusion in TiC, with a diffusion rate approximately 700 times greater at 1173 K, promoting Si diffusion into the interior of TiC grains.

CRediT authorship contribution statement

Qing Chang: Writing – original draft. **Qing Peng:** Writing – review

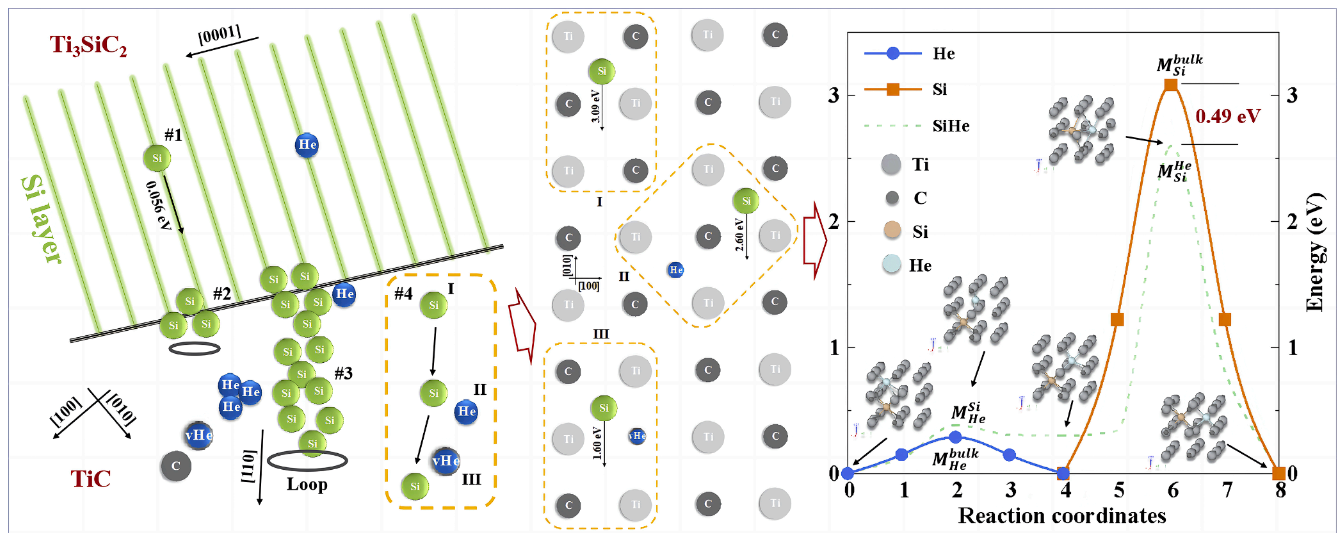

Fig. 15. Schematic diagram of the striped Si layer formation mechanism in TiC. (a) Comprehensive route of Si segregation from Ti_3SiC_2 to TiC. (b) Accelerated migration of Si interstitials in TiC enhanced by He interstitial and vacancy-He complex. (c) Detailed migration barriers and paths of Si interstitial, He interstitial, and SiHe cluster in bulk TiC. The site of interstitial He is shifted along ⟨100⟩ directions by 0.37 Å off the cubic center, which has 6 equivalent configurations. The migration barrier of the He interstitial inside the same cubic is calculated to be 0.016 eV.

& editing, Writing – original draft, Supervision, Investigation. **Jiannan Hao:** Writing – original draft, Methodology. **Pan Qi:** Supervision. **Penghui Lei:** Formal analysis. **Ni Jiang:** Formal analysis. **Chao Ye:** Writing – review & editing, Writing – original draft, Supervision, Investigation, Funding acquisition, Conceptualization.

Declaration of competing interest

The authors declare that they have no known competing financial interests or personal relationships that could have appeared to influence the work reported in this paper.

Data availability

No data was used for the research described in the article.

Acknowledgments

The authors acknowledge the financial support from the National Key R&D Program of China (Grant No. 2022YFB3707200); National Natural Science Foundation of China (Grant No. 12272378); National Science Fund for Distinguished Young Scholars of China (No. 12205236); High-level Innovation Research Institute Program of Guangdong Province (No. 2020B0909010003); LiYing Program of the Institute of Mechanics, Chinese Academy of Sciences (Grant No. E1Z1011001); Innovation Capability Support Program of Shaanxi (Program No.2023-CX-TD-45; Program No.2023KJXX-009).

References

[1] S.J. Zinkle, G.S. Was, Materials challenges in nuclear energy, Acta Mater 61 (3) (2013) 735–758.
[2] P. Yvon, F. Carré, Structural materials challenges for advanced reactor systems, J. Nucl. Mater. 385 (2) (2009) 217–222.
[3] K.R. Whittle, M.G. Blackford, R.D. Aughterson, S. Moricca, G.R. Lumpkin, D. P. Riley, N.J. Zaluzec, Radiation tolerance of $M_{n+1}AX_n$ phases, Ti_3AlC_2 and Ti_3SiC_2, Acta Mater 58 (13) (2010) 4362–4368.
[4] Z.M. Sun, Progress in research and development on MAX phases: a family of layered ternary compounds, Int. Mater. Rev. 56 (3) (2013) 143–166.
[5] C. Wang, C.L. Tracy, R.C. Ewing, Radiation effects in M_{n+1}AXn phases, Appl. Phys. Rev. 7 (4) (2020).
[6] M.W. Barsoum, The $M_{N+1}AX_N$ phases: a new class of solids: thermodynamically stable nanolaminates, Prog. Solid. State Ch. 28 (1) (2000) 201–281.
[7] S. Li, Z. Yang, R. Khaledialidusti, S. Lin, J. Yu, M. Khazaei, J. Zhang, L. Sun, X. Li, W. Su, High-throughput study and machine learning on MAX and MAB phases: new materials and fingerprints of superior lattice thermal conductivities, Acta Mater 254 (2023) 119001.
[8] J. Xie, X. Wang, A. Li, F. Li, Y. Zhou, Corrosion behavior of selected $M_{n+1}AX_n$ phases in hot concentrated HCl solution: effect of A element and MX layer, Corros. Sci. 60 (2012) 129–135.
[9] R. Radhakrishnan, J.J.WM. Akinc, Synthesis and high-temperature stability of Ti3SiC2, J. Alloys Compd 285 (1999) 85–88.
[10] M.A. Tunes, S.M. Drewry, J.D. Arregui-Mena, S. Picak, G. Greaves, L.B. Cattini, S. Pogatscher, J.A. Valdez, S. Fensin, O. El-Atwani, S.E. Donnelly, T.A. Saleh, P. D. Edmondson, Accelerated radiation tolerance testing of Ti-based MAX phases, Mater. Today Energy 30 (2022) 101186.
[11] C. Ye, Q. Chang, P. Lei, W. Dong, Q. Peng, Microstructure evolution in Si^+ ion irradiated and annealed Ti_3SiC_2 MAX phase, J. Am. Ceram. Soc. 105 (9) (2022) 5921–5928.
[12] Q. Qi, G.J. Cheng, L.Q. Shi, D.J. O'Connor, B.V. King, E.H. Kisi, Damage accumulation and recovery in C^+-irradiated Ti_3SiC_2, Acta Mater 66 (2014) 317–325.
[13] H.H. Shen, F.Z. Li, H.B. Zhang, S.M. Peng, X.T. Zu, K. Sun, Effects of Xe^+ irradiation on Ti_3SiC_2 at RT and 500°C, J. Eur. Ceram. Soc. 37 (2) (2017) 855–858.
[14] D.W. Clark, S.J. Zinkle, M.K. Patel, C.M. Parish, High temperature ion irradiation effects in MAX phase ceramics, Acta Mater 105 (2016) 130–146.
[15] T. Yang, C. Wang, W. Liu, S. Liu, J. Xiao, Q. Huang, J. Xue, S. Yan, Y. Wang, Formation of nano-twinned structure in Ti_3AlC_2 induced by ion-irradiation, Acta Mater 128 (2017) 1–11.
[16] C. Wang, T. Yang, C.L. Tracy, J. Xiao, S. Liu, Y. Fang, Z. Yan, W. Ge, J. Xue, J. Zhang, J. Wang, Q. Huang, R.C. Ewing, Y. Wang, Role of the X and n factors in ion-irradiation induced phase transformations of $M_{n+1}AX_n$ phases, Acta Mater 144 (2018) 432–446.
[17] C. Wang, T. Yang, C.L. Tracy, C. Lu, H. Zhang, Y.J. Hu, L. Wang, L. Qi, L. Gu, Q. Huang, J. Zhang, J. Wang, J. Xue, R.C. Ewing, Y. Wang, Disorder in $M_{(n+1)}AX_{(n)}$ phases at the atomic scale, Nat. Commun. 10 (1) (2019) 622.
[18] T. Yang, C. Wang, C.A. Taylor, X. Huang, Q. Huang, F. Li, L. Shen, X. Zhou, J. Xue, S. Yan, Y. Wang, The structural transitions of Ti_3AlC_2 induced by ion irradiation, Acta Mater 65 (2014) 351–359.
[19] J.C. Nappé, C. Maurice, P. Grosseau, F. Audubert, L. Thomé, B. Guilhot, M. Beauvy, M. Benabdesselam, Microstructural changes induced by low energy heavy ion irradiation in titanium silicon carbide, J. Eur. Ceram. Soc. 31 (8) (2011) 1503–1511.
[20] H.F. Zhang, B.D. Yao, L.Q. Shi, D.J. O'Connor, J. Huang, J.Y. Zhang, W. Ding, Y. X. Wang, Roles of silicon-layer in Ti_3SiC_2 materials response to helium irradiation: new insights from first-principles calculation, Acta Mater 97 (2015) 50–57.
[21] B. Yao, G. Hu, Z. Yu, H. Zhang, L. Shi, H. Shen, Y. Wang, Effect of H and He on the mechanical properties of Ti_3SiC_2: the first-principles calculation, Acta Phys. Sin 65 (2) (2016) 026202.
[22] Q. Song, P. Zhang, J. Zhuang, X.-J. Ning, Migrating and clustering of He atoms in Ti_3SiC_2: first-principles calculations, Comput. Mater. Sci. 137 (2017) 327–331.
[23] H. Zhang, R. Su, I. Szlufarska, L. Shi, H. Wen, Helium effects and bubbles formation in irradiated Ti_3SiC_2, J. Eur. Ceram. Soc. 41 (1) (2021) 252–258.
[24] R. Su, L. Shi, J.H. Perepezko, H. Zhang, Helium-driven element depletion and phase transformation in irradiated Ti_3SiC_2 at high temperature, J. Eur. Ceram. Soc. 43 (8) (2023) 3104–3111.
[25] W.A. Hanson, M.K. Patel, M.L. Crespillo, F. Zhang, S.J. Zinkle, Y. Zhang, W. J. Weber, Ionizing vs collisional radiation damage in materials: separated, competing, and synergistic effects in Ti_3SiC_2, Acta Mater 173 (2019) 195–205.
[26] G. Kresse, J. Furthmüller, Efficient iterative schemes for ab initio total-energy calculations using a plane-wave basis set, Phys. Rev. B 54 (16) (1996) 11169–11186.
[27] J.P. Perdew, Y. Wang, Accurate and simple analytic representation of the electron-gas correlation energy, Phys. Rev. B 45 (23) (1992) 13244–13249.
[28] G.A. Henkelman, B.P. Uberuaga, H.J.J.o.C.P. Jónsson, A climbing image nudged elastic band method for finding saddle points and minimum energy paths, J. Chem. Phys. 113 (2000) 9901–9904.
[29] R. Su, H. Zhang, L. Liu, L. Shi, H. Wen, Reversible phase transformation in Ti_2AlC films during He radiation and subsequent annealing, J. Eur. Ceram. Soc. 41 (13) (2021) 6309–6318.
[30] S.J. Zinkle, Radiation-induced effects on microstructure**prepared for the oak ridge national laboratory under contract no. DE-AC05-000R22725, Comprehens. Nucl. Mater. (2012) 65–98.
[31] Y. Xu, X. Bai, X. Zha, Q. Huang, J. He, K. Luo, Y. Zhou, T.C. Germann, J. S. Francisco, S. Du, New insight into the helium-induced damage in MAX phase Ti_3AlC_2 by first-principles studies, J. Chem. Phys. 143 (11) (2015) 114707.
[32] J. Emmerlich, D. Music, P. Eklund, O. Wilhelmsson, U. Jansson, J.M. Schneider, H. Högberg, L. Hultman, Thermal stability of Ti_3SiC_2 thin films, Acta Mater. 55 (4) (2007) 1479–1488.
[33] J. Gao, H. Huang, J. Liu, R. Liu, Q. Lei, Y. Li, Synergistic effects on microstructural evolution and hardening of the Hastelloy N alloy under subsequent He and Xe ion irradiation, J. Appl. Phys. 123 (20) (2018) 205901.
[34] J. Liu, H. Huang, A. Liu, Y. Li, The effects of post-irradiation isochronous annealing on defects evolution and hardening in Hastelloy N alloy, J. Nucl. Mater. 548 (2021) 152855.
[35] Z.D. Jastrzebaski, The Nature and Properties of Engineering Materials, 2nd ed., United States of America, 1976.
[36] S. Jin, L. Guo, Y. Ren, R. Tang, Y. Qiao, TEM Characterization of Self-ion Irradiation Damage in Nickel-base Alloy C-276 at Elevated Temperature, J. Mater. Sci. Technol. 28 (11) (2012) 1039–1045.
[37] J. Xiao, T. Yang, C. Wang, J. Xue, Y. Wang, S. Sinnott, Investigations on Radiation Tolerance of $M_{n+1}AX_n$ Phases: study of Ti_3SiC_2, Ti_3AlC_2, Cr_2AlC, Cr_2GeC, Ti_2AlC, and Ti_2AlN, J. Am. Ceram. Soc. 98 (4) (2015) 1323–1331.
[38] S.C. Middleburgh, G.R. Lumpkin, D. Riley, Y. Zhon, Accommodation, Accumulation, and Migration of Defects in Ti_3SiC_2 and Ti_3AlC_2 MAX Phases, J. Am. Ceram. Soc. 96 (10) (2013) 3196–3201.
[39] C. Xu, H. Zhang, S. Hu, X. Zhou, S. Peng, H. Xiao, G. Zhang, First-principles calculations of Ti_3SiC_2 and Ti_3AlC_2 with hydrogen interstitial, J. Nucl. Mater. 488 (2017) 261–266.
[40] T. Li, T. Liu, L. Zhang, T. Fu, H. Wei, First-principles investigation on slip systems and twinnability of TiC, Comput. Mater. Sci. 126 (2017) 103–107.
[41] J. Hao, S. Jin, G.H. Lu, H. Xu, Migration energy barriers and diffusion anisotropy of point defects on tungsten surfaces, Comput. Mater. Sci. 184 (2020) 109893.
[42] G.E. Vineyard, Frequency factors and isotope effects in solid state rate processes, J. Phys.Chem. Solids 3 (1957) 121–127.